Assessment of the 1-fluid method for DNS of particulate flows: Sedimentation of a single sphere at moderate to high Reynolds numbers

G. Pianet [a,*], A. Ten Cate [b], J.J. Derksen [c], E. Arquis [a]

[a] *Laboratoire Transferts Écoulements Fluides Énergétique site ENSCPB, UMR CNRS 8508, 16 Av. Pey-Berland, 33607 PESSAC, France*
[b] *Department of Chemical Engineering, Princeton University, Princeton, NJ 08540, USA*
[c] *Kramers Laboratorium voor Fysische Technologie, Delft University of Technology, Prins Bernhardlaan 6, 2628 BW Delft, The Netherlands*

Abstract

This paper introduces an original 1-fluid method for direct simulation of the motion of rigid particles in fluids. The model is based on the implicit treatment of a single fictitious fluid over a fixed grid, and uses an augmented Lagrangian optimization algorithm for the velocity–pressure coupling. The paper focuses on the case of a rigid sphere settling in a viscous medium. For validation purposes, simulations of the transient motion of a sedimenting sphere at Reynolds numbers ranging from 1.5 to 31.9 are compared to the PIV data published by Ten Cate et al. [Ten Cate A, Nieuwstad CH, Derksen JJ, Van den Akker HEA. Particle imaging velocimetry experiments and lattice-Boltzmann simulations on a single sphere settling under gravity. Phys Fluids 2002;14(11):4012–25]. Accurate reproduction of the experimental data is obtained. Further simulations are intended to investigate higher Reynolds numbers. Predictions of transient particle sedimentation at Reynolds number 280 are performed and compared with experimental data of the sedimentation trajectory, as well as with simulation results based on the lattice-Boltzmann method.
© 2006 Elsevier Ltd. All rights reserved.

1. Introduction

The problem of predicting interactions between hard particles and a surrounding viscous fluid concerns many industrial and environmental domains. The processing of sophisticated fuels, foodstuffs, cosmetics or the transport of aerosols in environmental flows are some examples.

The physical behavior of these flows is roughly characterized by the Reynolds number regime, the density of each of the phases and the liquid/solid volume fraction. These parameters are used to evaluate the strength of the interactions between the liquid and solid phases. In recent literature, many numerical approaches have tended to take strong fluid/particle interactions into account. As an exam-

ple, some of the early computational approaches to disperse flows are the Eulerian/Eulerian two-fluid methods. These techniques treat each of the phases as a single equivalent fluid, and empirical coupling relations are used. The latter methods yield good results when the scale of the computational domain is far larger than the scale of the particle. The increasing performance of computers has recently driven the modelling efforts to focus on direct numerical simulation (DNS) methods. In DNS, every flow scale can be captured at the expense of high spatial and temporal resolution. This is made possible through the explicit modelling of fluid/particle boundaries so that the bilateral actions between both of the phases are computed without empirical coupling.

This paper presents a DNS-related method for simulating the transient motion of rigid bodies in a viscous fluid. The challenge lies in a reliable modelling of the liquid–solid coupling over a wide range of Reynolds numbers.

---

* Corresponding author. Tel.: +33 540 006 682; fax: +33 540 006 668.
E-mail address: gregoire.pianet@free.fr (G. Pianet).
URL: http://gregoire.pianet.free.fr/Research.html (G. Pianet).

An overview of existing DNS approaches points out two propensities related either to unstructured moving meshes or to fixed Cartesian meshes.

In the first case, the interface is considered as a moving boundary condition. An example lies in the arbitrary Lagrange–Euler methods (ALE) where fluid and solid momentum equations are combined together. Much of the ALE method was provided by Hu et al. [18]. The time and space dependent meshes are useful in the case of drop and bubble modelling, as is attested in the recent paper of Legendre et al. [24]. Yet, these methods involve costly remeshing and the three dimensional implementation remains manifestly difficult.

In the second case, many authors have proposed techniques involving computing a Lagrangian tracking of the dispersed phase on meshes fixed in time and space. For an example we refer the reader to the front-tracking methods (see [29]) and much earlier with the Marker and cell volume tracking method (see [14]). Another way to model liquid–solid suspensions on stationary meshes is the fictitious domain approach developed by Glowinski et al. [12]. The solid motion is ensured by a penalty technique based on distributed Lagrange multipliers (DLM) at the interface level. The efficiency of the DLM method has been proven in many cases like sedimentation of rigid bodies and fluidization [12], or particle transport in pressure driven channel flow [13].

In our research, we use the 1-fluid method (1F), that was recently developed by Caltagirone and Vincent [3] who was inspired by volume penalty methods in fictitious domains [20] and interface reconstruction [30]. The term ''1-fluid'' means that fluid and solid phases are considered as a single equivalent fluid in the sense of the Navier–Stokes equations. The equivalent fluid requires equivalent densities and viscosities depending on time and space by means of a phase function. The latter indicates whether the considered grid node belongs to fluid or solid phase, and drives the coupling of the Navier–Stokes equations with the interface transport equation. The following features make the 1F method very attractive for simulating particles in fluid; (i) Using phase function allows to use fixed Cartesian grids, which is computationally practical. (ii) The same set of equations is solved in both dispersed and continuous phases and the interface between the phases is only tracked implicitly. As a result the computational effort does not scale with the number of particles. (iii) The tensorial penalty method [26] used to ensure both the incompressibility constraint in the fluid phase and the non-deformability constraint in the solid is just based upon two parameters defined from the characteristic flow scales. (iv) For solving the velocity–pressure coupling, the augmented Lagrangian algorithm [11] is used in all phases. This results in a stable and efficient technique.

An alternative method used for the direct simulation of suspended particles is the lattice-Boltzmann method (LB). This method has been introduced some 15 years ago as an alternative method for the computation of fluid motion.

The fluid is represented by mass that propagates on an equidistant cubic grid at discrete time steps. By applying collision rules that conserve mass and momentum, it can be demonstrated that the macroscopic system obeys the continuity and Navier–Stokes equations for incompressible flow.

A main advantage of this method is that scalability on parallel computer platforms is excellent because most operations are local. For a background on the method we refer the reader to [6,7,33]. Application of the LB method to simulations of particles in fluid has been first proposed by [22,23]. The good scalability of the method has made the LB method quite popular for numerical studies of particle–fluid interactions. Some examples of recent studies are [5,15,16]. In the recent paper of Ten Cate et al. [4], LB simulations of the sedimentation of a single sphere in the range $1.5 < Re_p < 31.9$ are compared with experimental data. Here we define the particle Reynolds number in the same way, i.e. $Re_p = \rho_f u_\infty d_p / \mu_f$; ($\rho_f$: fluid density, μ_f: fluid dynamic viscosity, d_p: particle diameter, u_∞: particle terminal settling velocity).

The purpose of this paper is to validate classical benchmarks and fully resolve unsteady simulations with a view to built confidence about the implicit tracking of fluid–solid interfaces via a viscosity-based penalty method. The first step is to perform validations of the 1F method against the experimental data of Ten Cate et al. [4] in the Reynolds number range $1.5 < Re_p < 31.9$. The next step is to compare Ten Cate's LB simulations, our 1F simulations and experimental data from Mordant and Pinton [25] at a Reynolds number of 280. Concerning validations, we draw heavily on two experimental results.

In the first case, particle imaging velocimetry (PIV) experiments from Ten Cate et al. [4] concerning the case of a sphere settling at Reynolds numbers Re_p ranging from 1.5 to 31.9. Ref. [4] is actually one of the few papers where the particle and domain sizes, the moderate regimes and the measurement techniques are all designed for good validation of DNS methods. The validation is focused on both fluid and particle transient behavior. The LB simulations described in the same paper match the experiments accurately.

In the second case, the experiments from Mordant and Pinton [25] give the velocity of a settling particle by measuring the Doppler shift of scattered ultrasound. The resulting particle velocity time series are shown to be correctly fitted by a single exponential relation within the particle Reynolds number range that runs from 40 to 8000.

A description of the 1F methodology and the way in which its numerical parameters are set is described in the following section. As a validation step, the experimental data from [4] are compared with 1F simulations in Section 3. In Section 4, the experiments from [25] are briefly described and applied to the cross-validation of both 1F and LB simulations concerning the sedimentation of a single particle at a Reynolds number $Re_p = 280$. Comparisons of the methods' efficiency and modularity are discussed in the conclusion.

2. Numerical methodology

This section gives details about the problem statement and presents the computational aspects of the 1F method.

2.1. 1-Fluid model

A way in which the problem can be expressed reads

$$\rho\frac{\partial \mathbf{u}}{\partial t} + \rho(\mathbf{u} \cdot \nabla)\mathbf{u} = \rho\mathbf{g} - \nabla p + \nabla \cdot (\mu(\nabla\mathbf{u} + \nabla^{\mathrm{t}}\mathbf{u})), \qquad (1)$$

$$\frac{\partial C}{\partial t} + \mathbf{u} \cdot \nabla C = 0, \qquad (2)$$

$$\nabla \cdot \mathbf{u} = 0, \qquad (3)$$

where (1) is the momentum conservation, (2) the equation of advection applied to the phase function C and (3) the continuity equation. We have to define the spatial and temporal evolution of the volume fraction solid/fluid $C(\mathbf{x}, t)$ which could be extended to the case of N immiscible phases: $C = \sum_{i=1}^{N} C_i$, C_i being the specific volume fraction attached to the ith phase.

The results presented in this paper are restricted to the case of a single solid phase. Consequently a Cartesian grid is used where the volume fraction field $C(\mathbf{x}, t)$ represents the multiphase topology of the flow. Thus D indicates the domain, ∂D its boundary, D_{f} the liquid phase, and D_{p} the solid phase. So if $M(\mathbf{x}, t)$ is a point of the field, the equivalent volume fraction reads

$$\begin{cases} C(\mathbf{x}, t) = 0 & \text{if } M \in D_{\mathrm{f}}, \\ C(\mathbf{x}, t) = 1 & \text{if } M \in D_{\mathrm{p}}. \end{cases} \qquad (4)$$

After discretization, the interface can be located where the phase function is $C = 0.5$. The equation of advection (2) applied to the phase function C ensures the interface displacement. These equations are available in both fluid and solid phases. Finally one must add the equations of state for μ and ρ. Note that in Eq. (1) the dynamic viscosity μ is not expressed as a pre-factor of a Laplacian term since both viscosity and density ρ depend on space. The equivalent fluid is incompressible with both ρ and μ depending on time and space. In fact, if a Lagrangian tracking is performed on any equivalent fluid particle, the associated density keeps its initial value. As a consequence the equivalent density obeys

$$\frac{\mathrm{D}\rho}{\mathrm{D}t} = 0. \qquad (5)$$

Furthermore the mass conservation must be obeyed in the whole equivalent fluid and it reads classically

$$\frac{\mathrm{D}\rho}{\mathrm{D}t} + \rho(\nabla \cdot \mathbf{u}) = 0. \qquad (6)$$

The combination of Eqs. (5) and (6) shows that the whole velocity field must be divergence free. Both density ρ and viscosity μ are chosen as functions depending on C. A simple linear function of interpolation [2] is used:

$$\mu(\mathbf{x}, t) = \mu_{\mathrm{f}}(1 - C(\mathbf{x}, t)) + \mu_{\mathrm{p}}C(\mathbf{x}, t), \qquad (7)$$

$$\rho(\mathbf{x}, t) = \rho_{\mathrm{f}}(1 - C(\mathbf{x}, t)) + \rho_{\mathrm{p}}C(\mathbf{x}, t). \qquad (8)$$

Interpolations of physical parameters are also necessary within the spatial discretization. In that case, Eq. (8) is still employed but Eq. (7) is unavailable when large viscosity gradients occur. By using a harmonic mean,

$$\mu(\mathbf{x}, t) = \frac{\mu_{\mathrm{p}}\mu_{\mathrm{f}}}{(1 - C(\mathbf{x}, t))\mu_{\mathrm{p}} + C(\mathbf{x}, t)\mu_{\mathrm{f}}}, \qquad (9)$$

the interpolation of viscosity over mixed cells is now compatible with the viscous stress continuity [27]. Once the fluid dynamic viscosity μ_{f}, the fluid density ρ_{f} and the solid density ρ_{p} are defined according to the physical properties, the free parameter μ_{p} must be chosen of a sufficiently large value in order to ensure the undeformability condition. The latter is satisfied when the deformation tensor, $\overline{\overline{D}}$ approaches the zero tensor:

$$D_{ij} = \frac{1}{2}\left(\frac{\partial u_i}{\partial x_j} + \frac{\partial u_j}{\partial x_i}\right) \approx 0, \quad \forall M \in D_p, \ \ i, j = 1, 2, 3 \qquad (10)$$

with the velocity directions u_1, u_2, u_3 and position x_1, x_2, x_3 related respectively to u_x, u_y, u_z and x, y, z.

In order to transport accurately the high gradients located on the fluid/particle interface, Eq. (2) is solved by means of the hybrid geometrical/Lagrangian VOF piecewise linear interface construction (PLIC) method of Youngs et al. [36]. The phase function gradient gives the normal to the particle surface in each of the interfacial cells. The latter surface is divided into planes placed in each control volume (see Section 2.2) and advected through the fixed mesh. The algorithm comes to an end by computing the new volume fraction within each control volume. To sum up, the VOF-PLIC method is a geometrical way to solve Eq. (2) that assures that the interface thickness is restricted to the size of a single cell.

2.2. Computational method

To solve the system of Navier–Stokes equations, and in particular the velocity–pressure coupling, the augmented Lagrangian (AL) method based on Uzawa's iterative method for saddle point problems [11] is used. A vectorial projection method [2] is used as a correction step to improve the fluid incompressibility.

For time discretization of the Navier–Stokes equations, a semi-implicit formulation of the left-hand side of (1) is used following the discretization $\rho\frac{u^{n+1}-u^n}{\Delta t} + \rho(u^n \cdot \nabla)u^{n+1}$, where the non-linear convective term has been linearized by replacing u^{n+1} by u^n. There is no CFL restriction on the time and space steps like those required when using an explicit discretization. The time scheme applied to the transient term estimation is first-order accurate. Second-order accurate time schemes can be used instead but the AL algorithm tends to reduce the global order to unity.

The spatial discretization is done by means of a finite volume method on a staggered mesh (see [14]), i.e. a pressure node is defined at the center of a control volume, and velocity components are defined at the centers of the control volume faces. All of the terms are approximated by a second-order accurate centered spatial scheme, well known for its accuracy [17]. That scheme is also known to lead to numerical oscillations, but none of them were observed in our simulations.

The algebraic system, resulting from the discretization of the various equations on the staggered mesh, is pre-conditioned with a MILU method prior to its inversion done by means of an iterative BiCG-Stab technique [35].

The AL method is an iterative algorithm used to solve the velocity–pressure couple via a saddle-point method, and used for the coupling of the velocity components. It is formulated by adding, in Eq. (1), the constraint $r\nabla(\nabla \cdot \mathbf{u})$ where r is a penalty parameter usually kept constant over space and time. It is shown that r should exceed the greatest term in the conservation equation by 2 or 3 orders of magnitude. The problem lies in the choice of this term since our equivalent fluid is not homogeneous. Consequently a new technique called the adaptive augmented Lagrangian method [34] is applied. Starting from the characteristic scales u_0, L_0, t_0, p_0 and using a dimensionless constant M ranging from 10^2 to 10^3, the local penalty parameter r is defined as the solution of the equation

$$r(\mathbf{x}, t) = M \max \left(\rho L_0^2/t_0, \rho u_0 L_0, \rho L_0^2 g/u_0, p_0 L_0/u_0, \mu\right), \quad (11)$$

which discriminates the largest term in the conservation equation. This results in different values of r in the liquid and solid phases. Once r is defined, the classical AL algorithm reads

$$\mathbf{u}|^{k=0} = \mathbf{u}|^n, \quad p|^{k=0} = p|^n, \quad C|^{k=0} = C|^n. \quad (12)$$

$$\rho^{k=0}\left(\frac{\mathbf{u}^{k+1}}{\Delta t} + (\mathbf{u}^k \cdot \nabla)\mathbf{u}^{k+1}\right)$$

$$= \rho^{k=0}\mathbf{g} - \nabla p^k + \nabla \cdot [\mu^{k=0}(\nabla \mathbf{u}^{k+1} + \nabla^t \mathbf{u}^{k+1})]$$

$$+ \rho^{k=0}\left(\frac{\mathbf{u}^{k=0}}{\Delta t}\right) + r(\mathbf{x}, t)\nabla(\nabla \cdot \mathbf{u}^{k+1}), \quad (13)$$

$$p^{k+1} = p^k - r(\mathbf{x}, t)\nabla \cdot \mathbf{u}^{k+1}, \quad (14)$$

$$\mathbf{u}|^{n+1} = \mathbf{u}|^{k+1}, \quad p|^{n+1} = p|^{k+1}. \quad (15)$$

It is initialized in the equation set (12), where n is the global time step index and k the AL algorithm iteration number. The pressure calculation is done by accumulating the incompressibility constraint $r(\nabla \cdot \mathbf{u})$ in Eq. (14). Concerning the simulations in different regimes, the greatest contribution is first related to viscous forces so μ_f and μ_p are used to define r in the fluid phase and in the solid phase, respectively. When inertial effects overstep viscous ones, the convective term $\rho u_0 L_0$ is used instead of μ. As an example,

Table 1 gives our choice for the length, time and velocity scales used in the case of a sphere settling in a viscous media.

One can act on convergence via the BiCG-Stab iteration number but the penalty parameters used by the adaptative AL algorithm are also essential to respect at one and the same time the velocity–pressure coupling, velocity component coupling and mass conservation. In the fluid phase, M may be tuned so as to improve either the Navier–Stokes resolution ($M \to 10^2$) or the incompressibility constraint resolution ($M \to 10^3$). In the solid phase, $M = M_p$ drives the ratio μ_p/μ_f that acts on the coupling between the solid and liquid phases. In case of higher Reynolds number flows, the divergence of the flow field tends to increase. To prevent excessive increase, the vectorial projection technique of Caltagirone and Breil [2] is used to improve the fluid incompressibility. Boundary conditions on walls are implicitly enforced via additional terms in conservation equations. The way in which this contribution is used for several kinds of boundary conditions has been detailed for example in [34]. The sequence of operations of the 1F method are summarized in a general algorithm in Fig. 1.

Table 1
Setup of characteristic scales for a sphere settling in a viscous medium H, D and W are the three characteristic length scales of the domain

	Unsteady + inertial $\rho L_0^2/t_0$, $\rho u_0 L_0$	Gravity $\rho L_0^2 g/u_0$	Viscous constraint μ
u_0 (fluid)	$\langle u(\mathbf{x}, t)\rangle_{D_f}$	0	–
u_0 (solid)	$\langle u(\mathbf{x}, t)\rangle_{D_p}$	u_∞	–
L_0 (fluid)	H, D, W (domain)	0	–
L_0 (solid)	d_p	d_p	–
ρ (fluid)	ρ_f	ρ_f	–
ρ (solid)	ρ_p	ρ_p	–
μ (fluid)	–	–	μ_f
μ (solid)	–	–	μ_p
M (fluid)		M_f	
M (solid)		M_p	


```
n (global time step index)
  k (augmented Lagrangian iteration number)
    ┌─────────────────────────────────────────┐
    │ Setup of righthand side 'B'.            │
    │   (NS explicit & linearized terms)      │
    │ Setup of left–hand side 'A'.            │
    │   (Spatial discretization of NS eq. +   │
    │    AL terms)                            │
    │ Resolution of the linear system 'AX=B'  │      no
    │   via the BiCG–Stab solver.             │
    │ Pressure update.    ──▷ k=k+1           │──▷ k>k_max
    └─────────────────────────────────────────┘      yes
  Vectorial projection step.
  Interface advection (VOF–PLIC).
  Update of physical properties.
n=n+1
```
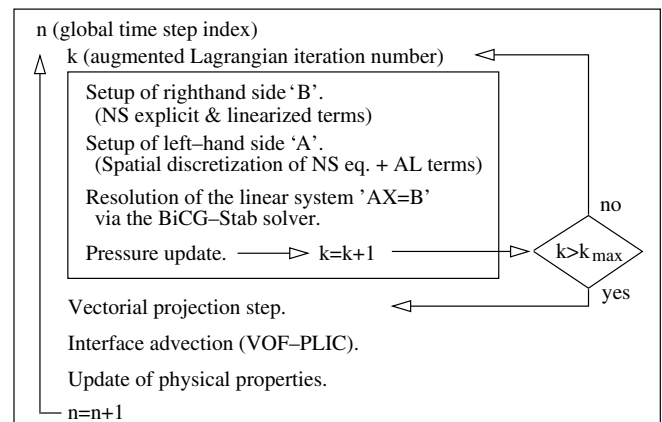
Fig. 1. Summarized algorithm for the 1F method.

2.3. Setup of numerical parameters

This section deals with the convergence in space and time of the 1F method. Apart from the spatial and temporal resolution, another critical parameter is the viscosity gradient located on the fluid/solid interface, and we must focus on the role the ratio μ_p/μ_f plays in the interfacial shape conservation. To our knowledge, there is almost no theoretical data about transient motion of spheres in a bounded fluid. Consequently, experimental results are used here to check 'a posteriori' the influence of both viscosity ratio and temporal resolution on the calculated solution. Concerning the convergence in space, our benchmark is based on analytical solutions of steady Stokes flows in ordered arrays of spheres. The last part shows to what extent the particle/wall interactions are reliable without explicit modelling of lubrication forces.

2.3.1. Convergence as function of the spatial resolution

This section deals with a 1F method validation case which is related to the Stokes drag on a sphere fixed in the laboratory frame. Many authors provided both theoretical and numerical results giving the drag force f as a function of the solid volume fraction c (e.g. Hasimoto (1959), Sangani and Acrivos (1982), Zick and Homsy (1982), we refer the reader to a comprehensive account of these papers by Hill et al. [15]). The computation is done over a fixed cubical unit-cell and a spherical obstacle whose radius is a located at its geometric center. All of the boundary conditions are periodic so that the domain is similar to a simple cubic array of spheres. The Cartesian mesh is fully defined by N which is the number of nodes per direction.

Fig. 2(a)–(c) depict three steady flows with $N = 80$ and solid volume fractions c ranging from 0.1 to 0.5. Streamlines are shown in particular flow slices. The contribution due to gravity does not affect the results and g is set to zero in the present simulations. The creeping flow is driven in the positive x direction by a uniform body force acting on the fluid that effectively mimics an average pressure gradient. The latter is chosen sufficiently weak so that the non-dimensional drag force dependency on Re_{Stokes} is as $F(Re_{Stokes}) = $ constant. F is defined as $F = f/f_{Stokes}$ where

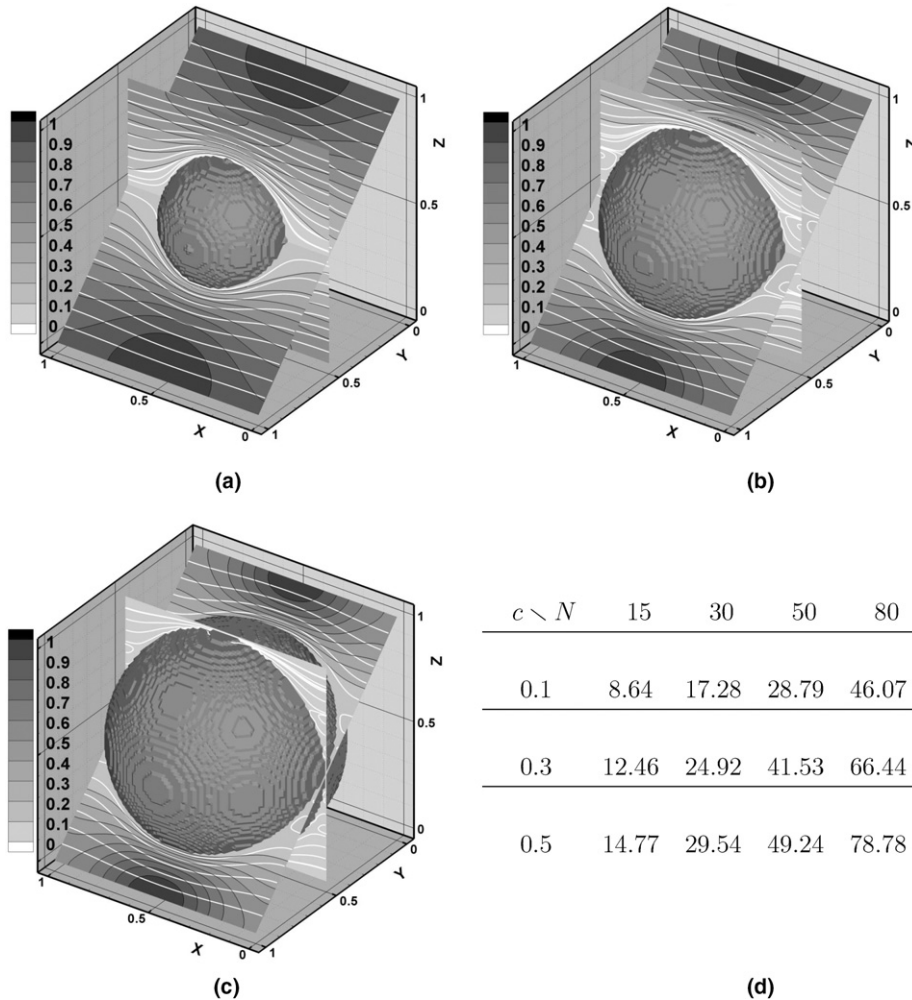| $c \searrow N$	15	30	50	80
0.1	8.64	17.28	28.79	46.07
0.3	12.46	24.92	41.53	66.44
0.5	14.77	29.54	49.24	78.78

Fig. 2. Contour levels of the relative velocity magnitude $|\mathbf{u}|/\max(|\mathbf{u}|)$ of Stokes flows in a simple cubic array of spheres. The flow is driven in the positive x direction by a uniform body force. The grid resolution is $N = 80$. Solid volume fractions are respectively $c = 0.1$ (a), $c = 0.3$ (b), $c = 0.5$ (c). Table (d) gives the number of grid units used in the sphere diameter for different values of (c, N).

f is the drag force on the sphere array and $f_{\text{Stokes}} = 6\pi\mu_{\text{f}}a\langle|\mathbf{u}|\rangle$ is the classical Stokes drag. Re_{Stokes} is based on the average velocity $\langle|\mathbf{u}|\rangle$ (integrated over the whole unit cell) so that $Re_{\text{Stokes}} = \rho_{\text{f}}\langle|\mathbf{u}|\rangle a/\mu_{\text{f}}$ (see [15]).

We are interested in the drag force convergence as the grid resolution increases. Fig. 3 points out the steady spatial convergence of the 1F method along with the solution of Zick and Homsy. The error increases with the solid volume fraction but decreases when the grid is refined. In fact at low volume fraction the convergence is related to the number of cells used to define the sphere. Toward high volume fractions, the convergence is related to the number of cells used to define the fluid phase. Fig. 4 compares the convergence rates at different solid volume fractions, where ε is the relative error of the 1F method. The method is shown to be first-order accurate in space.
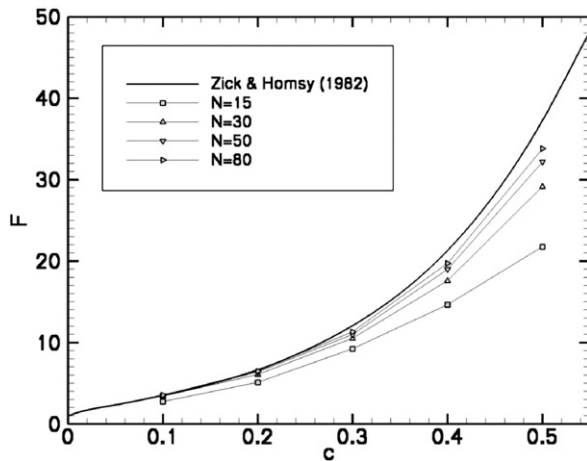
Fig. 3. Non-dimensional drag force F as a function of solid volume fraction c and spatial resolution N. The solid line is from Zick and Homsy, the symbols are from 1F simulations.
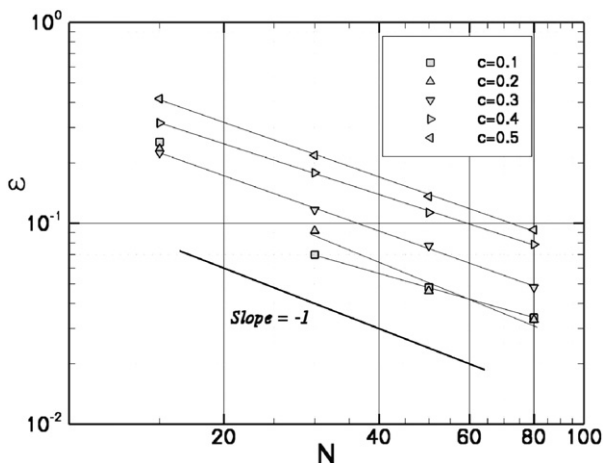

Fig. 4. Convergence rate of 1F simulations. Relative error ε versus spatial resolution N, as a function of the solid volume fraction c.

2.3.2. Convergence in time

The convergence study was performed with respect to experimental results (see Section 3) concerning the sedimentation of a sphere of diameter d_{p}.

The implicit integration used in the 1F method provides flexibility in the choice of time steps. Consequently a physical criterion based on characteristic times scales is required so as to avoid both over- and under-estimated discretizations. It is known that the particle relaxation time calculated from the Boussinesq–Basset–Oseen equation (see for example [32]):

$$T_a = \frac{2\left(\rho_p + \frac{1}{2}\rho_{\text{f}}\right)a^2}{9\mu_{\text{f}}}, \tag{16}$$

is based on both initial particle acceleration and terminal settling velocity, and that makes it a good estimator of the time it takes for the particle to reach its steady velocity. Consequently, the computational time step Δt [s] (see Section 2.2) is a constant chosen as a certain fraction α^{-1} of T_a (known also as the inertial time scale of particle acceleration).

Table 2 shows the evolution of $\Phi(\alpha) = u_{\text{p}}(T_a,\alpha)/u_\infty$ where $u_{\text{p}}(t,\alpha)$ denotes the instantaneous particle velocity at time t calculated with a time step $\Delta t = T_a/\alpha$, and u_∞ the steady-state velocity. Here the convergence is based on the sedimentation velocity at the specific time $t = T_a$ in the transient phase. The settling regime is defined by the particle Reynolds number $Re_{\text{p}} = 31.9$. Numerical results for various values of Δt are compared to the experimental one. Three different time steps Δt are chosen so as to range over one order of magnitude. Here it is shown that dividing the time step by 10 yields an error reduced by one order of magnitude. We use second-order time schemes but by adding the augmented Lagrangian algorithm, the method tends to be first-order accurate in time.

2.3.3. Impact of the viscosity ratio on the liquid–solid coupling

This section demonstrates the impact of the solid to liquid viscosity ratio $k = \mu_{\text{p}}/\mu_{\text{f}}$ on the particle behavior. Two extremes are found. In the former, when $\mu_{\text{p}} \to \mu_{\text{f}}$, the interface is subjected to strong deformations and in absence of surface tension models, it results in an underestimated particle drag. In the latter, that is to say $\mu_{\text{p}} \gg \mu_{\text{f}}$, the efficiency of the interpolation functions like (7) and the VOF algorithm convergence are both altered. As a consequence the solid penalty effects propagate to the flow next to the particle whose motion is slowed down. A correct calculation consequently requires the introduction of a balanced viscosity ratio. The convergence as a function of the viscosity ratio has been investigated starting from the

Table 2
Convergence in time

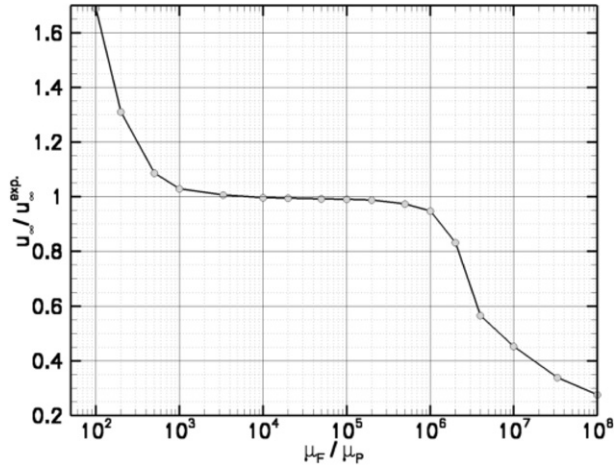| $\alpha = T_a/\Delta t$	138	276	1380	Exp.
$\Phi(\alpha)$	0.4323	0.4949	0.5362	0.5492
Error %	27.04	10.97	2.42	

Fig. 5. Effect of viscosity ratio k on the terminal settling velocity of a sphere at $Re_p = 31.9$. u_∞/u_∞^{exp} is the ratio between simulated and experimental terminal velocity.

Fig. 6. Dimensionless drag coefficient versus particle/wall gap. Numerical (1F) (—), analytical [10] (◇), $Re_p = 0.01$.

same validated data as those mentioned before (i.e. a sphere settling at $Re_p = 31.9$, see Section 3). Fig. 5 represents the evolution of the dimensionless settling velocity u_∞/u_∞^{exp} versus k. It is clear that the value of reference u_∞^{exp} is reached on a plateau that ranges roughly from 10^3 to 10^6.

2.3.4. Particle/walls interactions

By studying the lubrication effects involved in particle/wall interactions, the minimal gap width beyond which the 1F model is invalid is estimated. DNS methods do not implicitly require lubrication models when they keep large enough particle/particle or particle/wall separations. We chose to check the resolution limit by simulating a sphere settling under gravity towards a wall in the Stokes' regime.

Because of the long range action of viscous forces we need to use a large computational domain. For numerical efficiency the flow was simulated in an axisymmetric domain where the sphere moves along the axis of symmetry. In practice, the mesh is a square defined by 420×420 nodes. The boundaries are all of a no-slip kind except the symmetric one. The sphere is initially placed 10 diameters away from the top and bottom walls and 20 diameters from the side wall. The particle resolution is approximately 18 nodes per diameter and the expected particle Reynolds number is $Re_p = 0.01$. Once the acceleration phase is complete the error in the terminal settling velocity with respect to Stokes' velocity does not exceed 1%. Lubrication effects on approaching the bottom are represented in Fig. 6. Here the effect of the bottom wall on the particle is measured through the change in C_d/C_d^∞ where C_d is the drag coefficient, and C_d^∞ the Stokes drag coefficient in an unbounded medium. The sphere/bottom wall separation is expressed as the normalized gap $R = y_c/a - 1$, where y_c is the vertical coordinate of the particle center. By comparing that curve to the 'exact' theory of Brenner [1] confirmed by Elasmi et al. [10] one can see that the particle/wall interactions
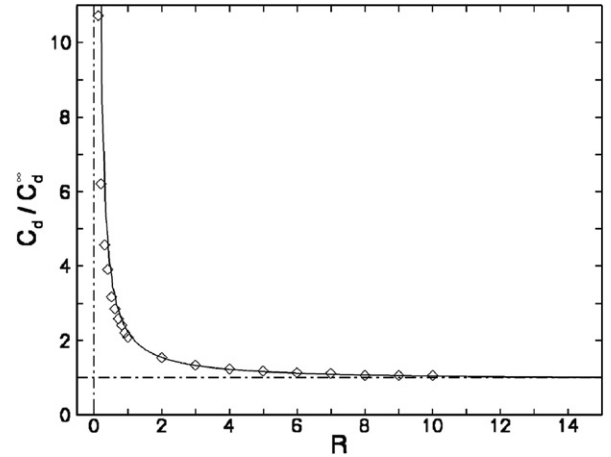
are correctly simulated until the gap reaches $R = 0.2$ or approximately $R = 2\delta$, when expressed in grid units δ. Past this gap, the simulated drag coefficient is significantly over-predicted. At this point, the two solutions are either to increase the grid resolution or to include sub-grid lubrication models. As noted above, such models are still in development and the results presented here are good enough for the scope of the paper.

Practically, the above results should help to set optimized numerical parameters prior to performing a simulation. The spatial convergence has been made clear here. Concerning low to moderate Re_p regimes and low volume fractions, roughly 10δ per particle diameter are necessary to provide quantitatively acceptable results, and there is no need for considering any radius calibration. A good approach for temporal resolution settings consists in choosing the time step Δt of the order of $\mathcal{O}(T_a/1000)$. Concerning the solid viscosity μ_p, a compromise respecting both transport scheme resolution and non-deformability conditions is to choose a ratio k ranging from 10^3 to 10^4.

3. Experimental setup and validations

The experimental configuration has been designed for the validation of LB direct numerical simulations. Settings and results are not presented in detail as they have been reported elsewhere (see [4]). As we focus first on the experimental characteristics required for the 1F method to be initialized, the simulation settings like spatial and temporal resolution and boundary conditions are justified. Finally the experimental results are presented in comparison to the 1F simulations.

3.1. Experimental setup

With respect to simulation constraints a wall-bounded geometry is set, and the particle's radius a is large enough, given that the spatial resolution of the simulation depends on the aspect ratio $2a/l$, where l is the length of the edge of

the domain's base (see Fig. 7). The container dimensions l, l, H are respectively 0.1, 0.1, 0.16 [m], the sphere diameter is $d_p = 0.015$ [m] and its density $\rho_p = 1120$ [kg/m³]. Reynolds numbers are modified as several silicon oils are successively used as fluid phases (see table in Fig. 7). Regarding the relevance of the classical rheology laws used for modelling these oils, we refer the reader to [4]. Different dimensionless parameters are introduced to qualify the physical behavior. The particle Reynolds number $Re_p = \rho_f \cdot u_\infty \cdot d_p/\mu_f$ is based on the upper velocity limit u_∞ of a sphere sedimenting in an unbounded medium. The particle Stokes number $St = 1/9 Re_p \rho_p/\rho_f$ which includes the density effects compares the response time of the particle to the characteristic time associated with the flow field. The particle's position is characterized by the dimensionless gap height h/d_p separating the sphere's bottom from the vessel's, and initially is set to 8. The initial distance separating the sphere's top from the free surface is roughly $1.7d_p$. There was no visible disturbances of the free surface during experiments. Both sphere and fluid velocities are normalized by u_∞. Experiments have been performed with three distinct Re_p values detailed in Fig. 7 where particle Reynolds numbers were calculated with help of the Abraham drag coefficients:

$$C_d = \frac{24}{(9.06)^2}\left(\frac{9.06}{\sqrt{Re_p}} + 1\right)^2. \tag{17}$$

PIV measurements were done in the acquisition plane represented in Fig. 7. Post-processed data consists of velocity fields picked-up for some acquisition frequencies ranging from 60 Hz to 248 Hz. Moreover, direct visualization, filtering and thresholding techniques are employed to extract the particle's trajectory. Note that an increase in resolution gives a decrease in frame size. So depending on the Re_p value, 3 or 4 camera frames are used successively, and it is required that the sphere be released from the initial position 3 or 4 times to capture the full trajectory. Finally, all experiments have been done twice to check reproducibility.

3.2. Simulation parameters setup

3.2.1. Boundary conditions

Fig. 8 depicts the four lateral boundary conditions. The tank's bottom is modeled by a no-slip condition. Concerning the free-surface of the tank, no-slip conditions have been set in the original LB simulations, but here it is considered more appropriate to set free-slip conditions.

To limit memory consumption, two symmetry boundary conditions are set in the flow. Theses conditions are located on two perpendicular planes whose intersection coincides with the sedimentation axis (see Fig. 8). This statement needs a justification: with these flow conditions in unbounded media, the particle Reynolds number is small enough for the flow to be laminar and inherently axisymmetric. In order to check that the square container does not alter our assumption, a computation was made on a $50 \times 50 \times 80$ mesh covering the whole physical domain. Fig. 9 compares the averaged radial component of velocity $\langle u_\parallel \rangle_y = \left\langle \sqrt{u_x^2 + u_y^2} \right\rangle_y$ to the averaged orthoradial component of velocity $\langle u_\perp \rangle_y = \left\langle \sqrt{u_z^2} \right\rangle_y$. The subscript y denotes the direction of averaging. These two quantities are calculated in a slice corresponding to the plane of symmetry $z = 0$ (see the origin of coordinates 'O' in Fig. 9). One can measure that the maximum ratio is $(\langle u_\perp \rangle_y < \frac{2}{100}(\langle u_\parallel \rangle_y)$ so that our hypothesis is numerically acceptable, keeping in mind that it would not be so with higher Re_p values where the particle's wake tends to be three-dimensional. An additional computation on a $51 \times 51 \times 82$ mesh was performed in order to verify that the non-zero $\langle u_\perp \rangle_y$ is not due to either an odd or even number of grid units in the particle diameter (see Fig. 9).

3.2.2. Impact of spatial and temporal resolution

Three simulations with increasing spatial resolution have been performed and compared to the experimental case $Re_p = 31.9$. A PIV slice is extracted when the dimensionless gap height $\frac{h}{d_p} = \frac{1}{2}$. Fig. 10 has been obtained by

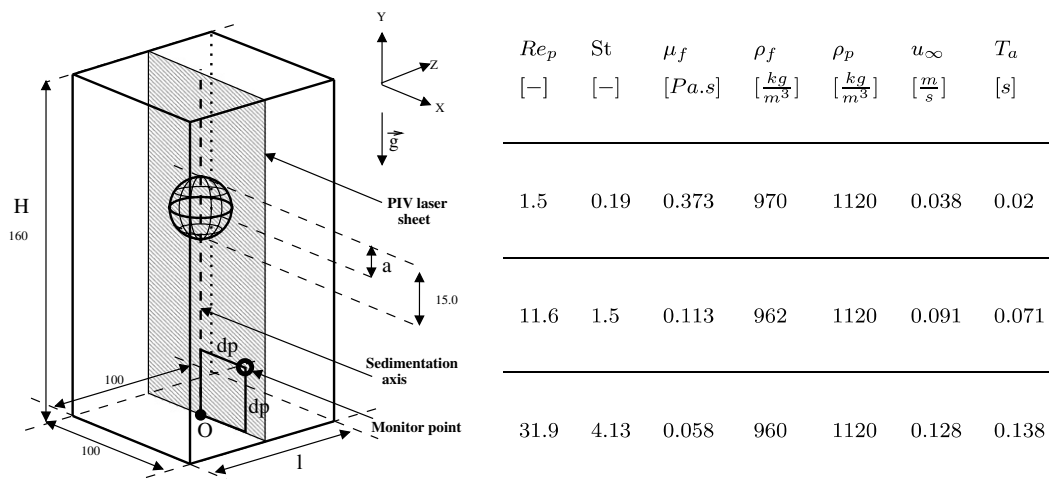| Re_p | St | μ_f | ρ_f | ρ_p | u_∞ | T_a |
[–]	[–]	[Pa.s]	[$\frac{kg}{m^3}$]	[$\frac{kg}{m^3}$]	[$\frac{m}{s}$]	[s]
1.5	0.19	0.373	970	1120	0.038	0.02
11.6	1.5	0.113	962	1120	0.091	0.071
31.9	4.13	0.058	960	1120	0.128	0.138

Fig. 7. Experimental settings: tank dimensions (mm) and physical parameters for three particle Reynolds numbers.
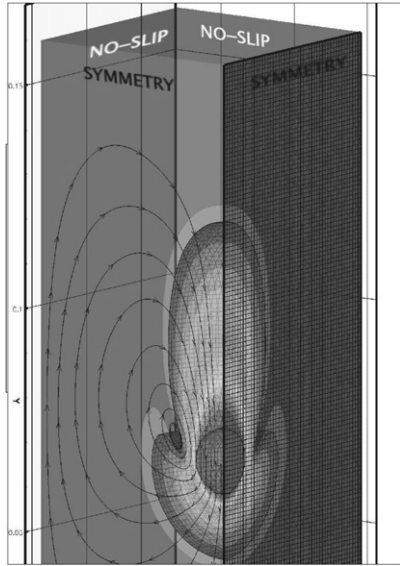
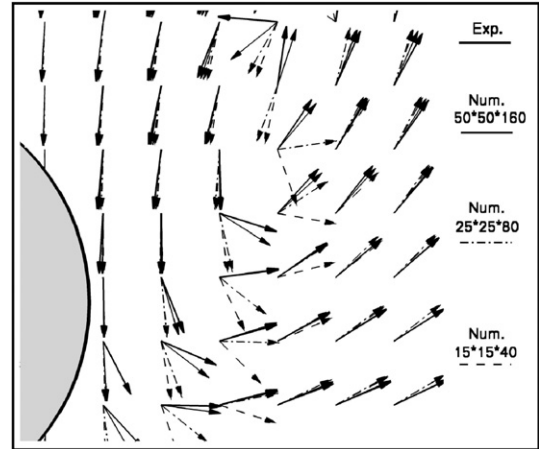Fig. 8. Overview of the computational domain.

Fig. 10. Spatial convergence of the velocity direction fields. Experimental (—), simulation: $160 \times 50 \times 50$ (—), $80 \times 25 \times 25$ (-·-·-), $48 \times 15 \times 15$ (- - -).
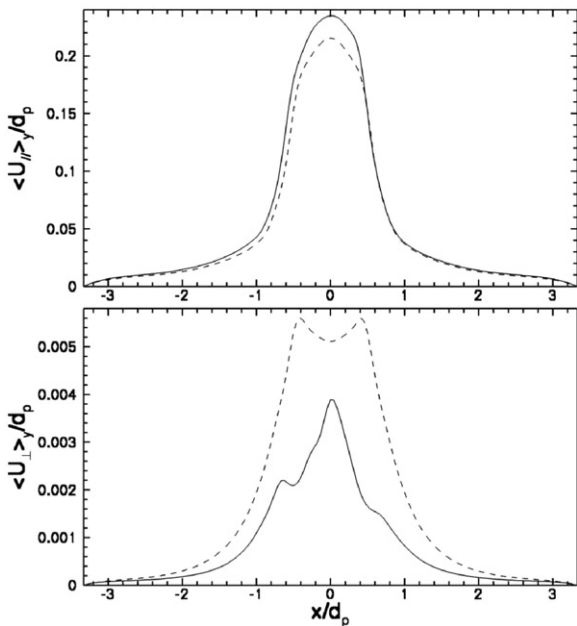
mentation of an adaptive mesh refinement in the 1F method.

In the following simulations, a resolution of $50 \times 50 \times 160$ grid units is used to represent a quarter domain (see Section 3.2) (i.e. a sphere diameter becomes 15δ). From our simulations at lower resolutions it was found that the global trajectory and velocity of the sedimenting sphere reproduced the experimental results well at a resolution of 7.5δ per diameter. Nevertheless, Fig. 10 shows that at higher resolution, the details of the simulated flow field still improved. Therefore, the highest resolution was chosen for further simulations.

The temporal resolution is defined by $\alpha = 1380$ so as to obtain a good accuracy. The resulting time step is adapted to the $Re_p = 31.9$ regime, but for reasons of computing time, we kept the resulting time step constant (i.e. $\Delta t = 1 \times 10^{-4}$ [s]) with the $Re_p = 1.5$ and $Re_p = 11.6$ regimes.

3.3. Comparison of experimental and 1F simulated results

The primary validation steps consist of reproducing the transient motion of the particle. Next the comparison is focused on the topology of the velocity field around the particle in its acceleration phase. Finally, time series are calculated on a fixed point of the fluid to check our method's accuracy for each of the velocity components independently.

3.3.1. Particle time series

The simulated cases are related to the three experiments detailed in Fig. 7. In Fig. 11 the simulation results are compared to the experimental data. At $Re_p = 1.5$ the steady state velocity reached by the particle is due to high viscous forces and to side-walls effects since the equivalent velocity in an unbounded medium is significantly higher (about 5%). With higher Reynolds numbers, these long-range interactions with walls progressively vanish, the particle reaching the bottom before its acceleration phase is being
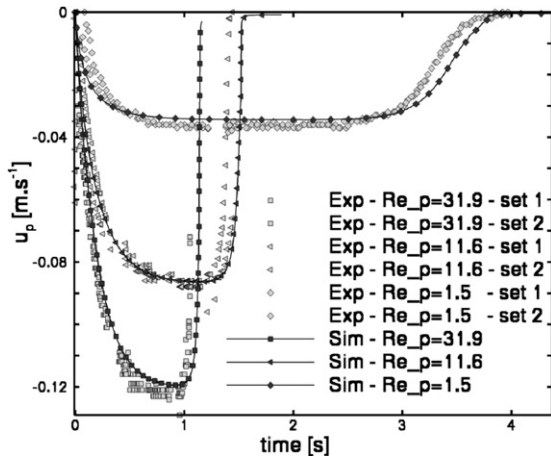

Fig. 9. Balance of radial and orthoradial velocity components on the symmetry planes. 1-Fluid simulations: (—) $50 \times 50 \times 80$, (- - -) $51 \times 51 \times 82$.

plotting the experimental and the three numerical fields on a single graph. It is shown that the vector field direction converges well to the experimental field, but that there is no global order of convergence. Indeed, one can see that in low-sheared zones all of the four vector fields are almost collinear, implying a very fast convergence. In the high-sheared zones, a continuous evolution from the low-resolution field to the high-resolution field is depicted, the latter being for each point of the fluid practically identical to the experimental field. This fact would justify the imple-

Fig. 11. Particle settling velocity, 1F simulations and measurements, $Re_\mathrm{p} = 1.5, 11.6, 31.9$.

achieved. Fig. 11 shows that the unsteady behavior is well reproduced by the 1F method. We may notice some imperfections by looking at the acceleration phase: the particle's velocity is slightly under-estimated so that a delay appears upon approaching the bottom, especially with low particle Reynolds numbers. This is certainly due to the fact that the simulations are under-resolved in time when decreasing the Re_p regime, so that α (see Section 2.3.2) is successively $\alpha_{(Re_\mathrm{p}=31.9)} = 1380$, $\alpha_{(Re_\mathrm{p}=11.6)} = 710$, $\alpha_{(Re_\mathrm{p}=1.5)} = 200$. Nevertheless the dynamic balance of the forces on the sphere is clearly validated.

3.3.2. Direction and magnitude of the velocity field

This section focuses on the evolution of the flow field along the particle's motion. In the previous paper [4], PIV slices were presented as frames issuing from a single camera position at a time. Here we are interested in the wake development during the acceleration phase, so we need to depict different camera frames simultaneously. Consequently one starts from the same initial data (i.e. untreated vector fields) to perform the complete top to bottom connections of the flow field. Comparisons over the three regimes are represented in Fig. 12 where the left part is a slice extracted from the three-dimensional simulation, the right one being the PIV slice. Each frame is a focus on the flow field surrounding the particle. Walls do not appear there.

An important feature to highlight is that each frame is a new measurement, and the result is that those frames could be connected in time very well as the wake extends continuously over different camera frames. As a consequence the reproducibility of the experiment is not to be called in question. Arrows in the figures indicate the flow direction. The frames where flow directions are incoherent and velocity magnitudes are very low, are dominated by experimental noise. In Fig. 12, views are picked at specific times $T_\mathrm{str} \simeq 0.1$ s, $T_\mathrm{acc} \simeq 0.5$ s and $T_\mathrm{std} \simeq 1$ s where the subscripts 'str', 'acc' and 'std' denote the startup phase, the acceleration phase and the steady-state phase respectively. The contour
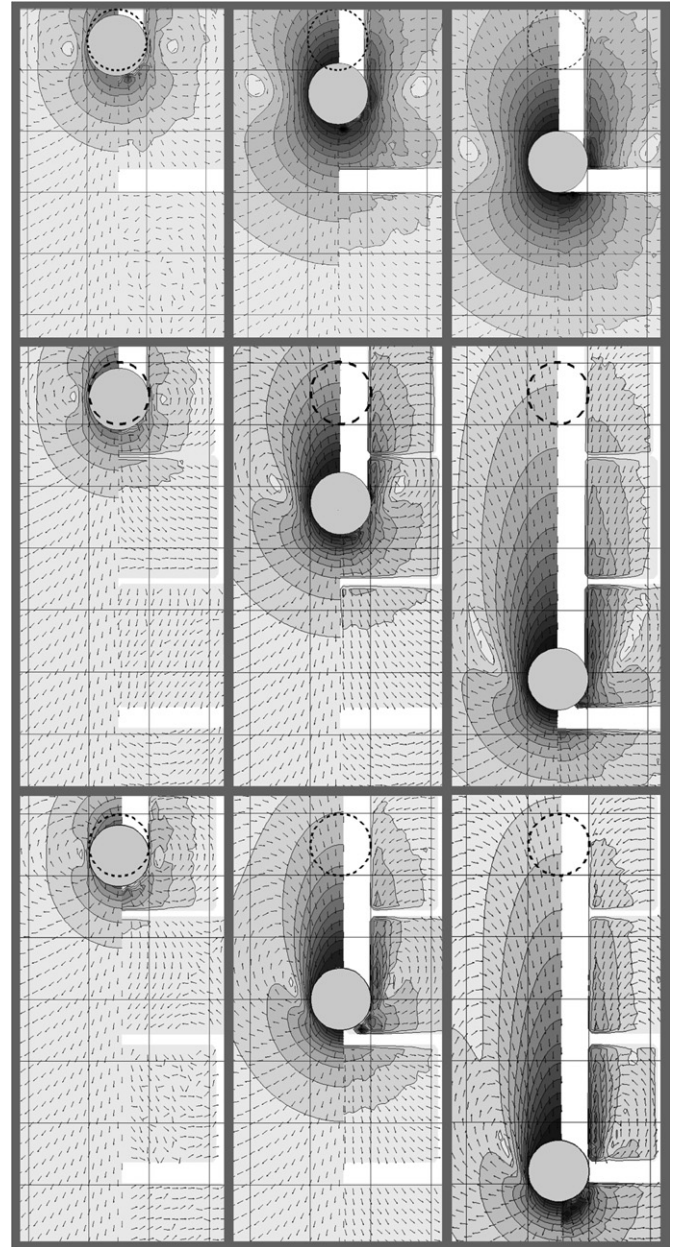

Fig. 12. Comparison of 1F method (left-hand side of each frame) and PIV slices (right-hand side of each frame). Contours of normalized velocity magnitude $|u|/u_\infty$, direction of velocity field. Re_p numbers are respectively 1.5, 11.6, 31.9 from top to bottom. Simulation/experimental times are respectively $T_\mathrm{str} \simeq 0.1$ s, $T_\mathrm{acc} \simeq 0.5$ s and $T_\mathrm{std} \simeq 1$ s from left to right.

levels correspond to the normalized velocity magnitude ranging from 0% to 100% of the terminal settling velocity. By comparing the two sides on each figure, it is shown that the numerical approach reproduces accurately the flow phenomena.

We may notice the inertial effects acting on the flow topology as Re_p increases: it appears that the lateral extension of the flow decreases while the wake is elongated. One may notice some structures elongated in the streamwise direction on the particle sides. These correspond to the vortex position in which velocities are very weak. This

curvature is clearly accentuated when the recirculation is stretched along the particle's trajectory by increasing Re_p. Such a phenomenon is explained by expressing Re_p as the ratio $Re_p = \tau_\nu/\tau_{p,a}$ where τ_ν is the diffusive time $\rho_f d_p^2/\mu_f$ and $\tau_{p,a} = d_p/u_\infty$ the advection time. This ratio decreases with increasing Re_p, indicating that at elevated Re_p, the momentum diffusion in the wake and on the particle sides is reduced compared to the particle advection.

3.3.3. Fluid time series

In this section, comparisons are performed by looking at the respective magnitude of each velocity component. The way that was dealt with in [4] was to set a monitor point one diameter away from the tank's bottom and one diameter away from the trajectory axis (the monitor point and the axis directions are depicted in Fig. 7).

Fig. 13(a)–(f) represents measured time series in the fluid $V_x(t)$ and $V_y(t)$ compared with what the 1F method predicts. By looking at V_x for the case $Re_p = 1.5$, one may see that there is an acceleration followed by a deceleration which coincides with the deceleration of the particle. This strong correlation due to viscous effects vanishes with higher Reynolds numbers. Indeed by looking V_x for $Re_p = 11.6$ and $Re_p = 31.9$, it occurs that once the particle stops, the fluid contained in the wake goes on moving around the particle, rejecting the initial vortex sideways. For example in Fig. 13(b), the first deceleration is related to the vortex core that gets closer to the monitor point, the consecutive acceleration being due to the inertial behavior of the wake that causes the vortex rejection. The last deceleration corresponds to dissipation of the kinetic energy in the fluid.

Comparison of results shows that these strong velocity fluctuations are very well predicted by our numerical method. Although the spatial resolution is the same over the three simulations, we may see that where the higher Reynolds numbers are well predicted, differences appear in fluid time series with $Re_p = 1.5$. Again these may be explained by a lack of temporal resolution as mentioned earlier in Section 3.3. There are also disruptions along the $Re_p = 1.5$ curves (see Fig. 13(a) and (d)) appearing just when the particle comes to a halt. These are due to weak inertial effects in the particle wake, maybe a consequence of the particle's velocity which is not correctly estimated as the particle/wall gap falls below 2 grid units. However, at this level, the experimental noise is too high to either confirm or invalidate the prediction.

4. Simulation of a single sphere settling at $Re_p = 280$: Cross-validation by means of 1-fluid and lattice-Boltzmann methods

In this section, the motion of a steel bead settling under gravity at a particle Reynolds number $Re_p = 280$ is simulated using both the 1F method and the LB method. The results are compared with the experimental data of Mordant et al. [25].

4.1. Experiment definitions

These experiments give the velocity of a settling particle by measuring the Doppler shift of scattered ultrasound. Measurements are performed in a tank filled with water at rest (container dimensions $H \times D \times W = 0.75 \times 1.1 \times 0.65$ [m], $d_p = 0.8$ [mm]). Mordant et al. [25] show that in
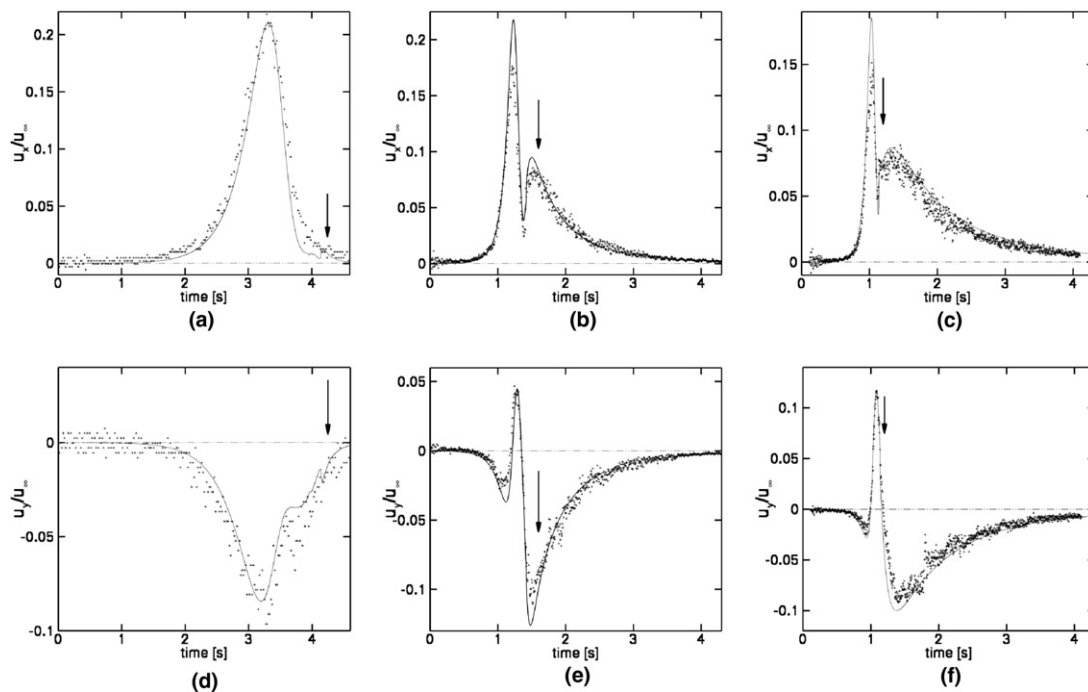

Fig. 13. Fluid time series for normalized velocity components u_x/u_∞ and u_y/u_∞. From left to right: $Re_p = 1.5$, 11.6 and 31.9. 1F (lines) and experimental (dots). Arrows indicate when the particle reaches the bottom of the tank.

Table 3
Experimental settings for $Re_p = 280$ [25]

Re_p (–)	St (–)	μ_f (Pa s)	ρ_f (kg/m^3)	ρ_p (kg/m^3)	u_∞ (m/s)	T_a (s)	τ_{95} (s)	d_{95} (m)
280	240	8.9×10^{-4}	1000	7710	$0.316 \pm 1\%$	0.328	0.108	0.0233

the range $40 < Re_p < 8000$, the particle's trajectory may be reproduced with the exponential law $u_p(t) = u_\infty(1 - \exp(3t/\tau_{95}))$, where τ_{95} is defined as the time it takes for the sphere to reach 95% of the terminal velocity. For the $Re_p = 280$ case, experimental data are summarized in Table 3, where d_{95} is the average distance covered by the particle during τ_{95}. Mordant et al. show that for the given Reynolds and Stokes number the particle sedimentation trajectory remains rectilinear.

4.2. 1F and LB Simulations setup

The LB simulations were done using the approach presented in [4]. While in lattice-Boltzmann simulations of moving particles generally the single relaxation BGK type LB scheme with bounce-back boundary conditions is used (see [22,23,6,7,33]), the method used and presented in this paper is slightly different. The lattice-Boltzmann scheme is based on the approach of Eggels and Somers [9,31]. This scheme is used for its enhanced numerical stability. The boundary condition of the sedimenting sphere is based on the adaptive force-field method of [8]. For further details the reader is referred to [4].

For our simulations, reproducing the entire experimental domain is not feasible. However, since the Re_p and St numbers are relatively high, the simulation domain can be taken much smaller than the experimental domain with minimal perceptible effect on the particle sedimentation trajectory. The experimental data show that 95% of the upper velocity limit is obtained after 0.0233 [m] of sedimentation. Therefore, the computational domain is taken as a box with dimensions $H \times D \times W = 0.064 \times 0.004 \times 0.004$ [m], with no-slip boundary conditions on all walls. With this height it is expected that a steady state velocity is achieved before the sphere reaches the bottom. Further, at this high Reynolds number it is expected that a relatively narrow containment has negligible impact on the sphere's sedimentation trajectory. In contrast to the 1F low Re_p simulations, the simulations are now done using the full sphere. All other physical parameters are set according to Table 3.

Several test simulations have been performed to set these parameters. It was found that the LB prediction improves as the spatial resolution increases and quantitatively acceptable results are found starting from $d_p = 16\delta$. In the same way, 1F predictions improve when the spatial resolution is successively defined as $d_p = 7\delta$, 8δ and 10δ, but there is no significant changes in both particle trajectory and velocity fields between $d_p = 8\delta$ and $d_p = 10\delta$. For the simulations reported below, the following settings are used and the computational efforts are shortly described:

Table 4
Overall characteristics for 1-fluid and lattice-Boltzmann simulation methods

	1F method	LB method
Advantages	Accuracy with few grid points, modularity	Numerically fast, second-order spatial schemes
Drawbacks	Computational cost	High resolution needed for accuracy, radius calibration

(i) *1F method*: A $800 \times 50 \times 50$ Cartesian grid ($d_p = 10\delta$) is used with a temporal resolution $\alpha = T_a/\Delta t = 4686$. The simulation required 3500 time steps and $N = 2 \times 10^6$ grid points. The resulting monoprocessor job was performed on a SGI Altix/3300 (12 cpus ia64 Madison/1300 MHz/L3/3Mo). It required 1225 h of CPU time and the memory used is evaluated as $N \times 300$(arrays of real numbers) $\times 8$(bits) ≈ 5 Gbytes.

(ii) *LB method*: A $1376 \times 86 \times 86$ Cartesian grid is used with a temporal resolution $\alpha = T_a/\Delta t = 24,095$. The particle diameter is $d_p = 16.0\delta$, and in a practical way $d_{p\,hydro} = 17.22\delta$ after the hydrodynamic radius calibration of the particle. The LB simulation required 20,000 time steps and $N = 10.2 \times 10^6$ grid points. The resulting job was performed via eight processors (MPI/900 MHz Pentium 3 linux system) and required 37 h of CPU time. The allocated memory was 143 Mbytes $\times 8$(processors) giving roughly 1.14 Gbytes total memory. The advantages and drawbacks for both of the methods are summarized in Table 4.

4.3. Simulation results

4.3.1. Velocities and trajectories comparison

The computed settling velocity $u_p(t)$ is represented in Fig. 14(a). Globally, our predictions match well with the expected transient behavior shown to be exponential in [25]. The 1F simulation results in a 2% underestimation of the terminal settling velocity u_∞, versus a 6% overestimation with the LB simulation, and a convergence to the experimental value was observed for both methods by increasing the spatial resolution. Consequently, the trajectories plotted in Fig. 14(b) match the experimental curve very well from time $t = 0$ [s] to time $t \simeq 0.22$ [s] when the particle reaches the solid bottom.

4.3.2. Flow field and wake structure comparison

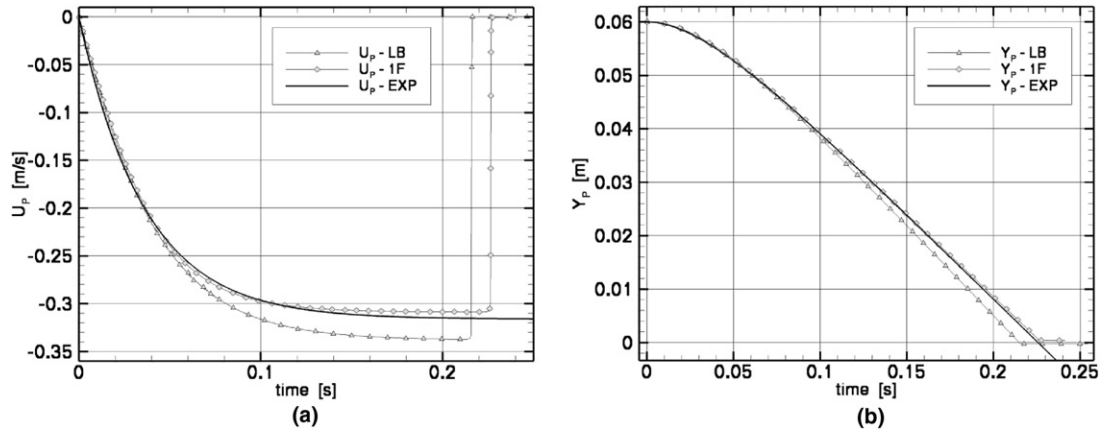Flow field slices are depicted in Fig. 15(a) (1F) and (b) (LB) at times $t = 0.028$, 0.091, 0.175 [s] and $t = 0.027$,

Fig. 14. (a) Settling velocity $u_p(t)$ at $Re_p = 280$, 1F method ($\diamond$), LB method ($\triangle$), exponential fit of averaged experimental values (bold line). (b) Particle trajectory $y_p(t)$ at $Re_p = 280$, 1F method ($\diamond$), LB method ($\triangle$), exponential fit of averaged experimental values (dashed line).

0.088, 0.177 [s], respectively. The contour levels correspond to $|u|/u_\infty$, the indexes refer to the vertical position divided by d_p while the black circle points out the release position. Some three-dimensional (1F) and in-plane (LB) streamlines are also depicted. By studying the spatial distribution of $|u|/u_p$ over the acceleration phase, one must notice the increasing backflow, and the steady upstream field. The two methods predict that the disturbed fluid is mainly located in a vertical cylinder whose diameter is similar to d_p. The difference lies in the bead's terminal velocity. Since the latter is under-estimated by the 1F method and over-estimated by the LB method, some more kinetic energy is transmitted from the particle to the fluid in the first case. This may explain why the steady-state wake extension is lower in the LB case.

The wake development is presented in more detail in Fig. 16(a) (1F Method) and (b) (LB Method). Both figures depict the axial distribution of velocity magnitude $|\mathbf{u}(\mathbf{x}_a, t)|/u_p(t)$, with $\mathbf{x}_a(x_a, z_a, y)$ the coordinates of the sedimentation axis (i.e. $\mathbf{x}_a(W/2, D/2, y)$). For improving readability, the evolution in time of the axial velocity magnitude is given in a frame of reference attached to the sphere motion. That moving frame of reference Y relates to the static frame according to the relationship $Y = y - y_p(t) + d_p/2$, such that the sphere center is fixed at $Y/d_p = 0.5$. For both the 1F and the LB method, the upstream profile is self-similar all along the instationary phase. The long range wake estimation is predicted as well. Right behind the sphere a back flow due to fluid inertia is noticed ($|u(t)|/u_p(t) > 1$). Locally, the prediction of the dynamic and static behavior differs according to the method used. The 1F method gives a monotonic increase of $|u(t)|/u_p(t)$ to the maximum fluid velocity u_m/u_∞. In the lattice-Boltzmann method $|u(t)|/u_p(t)$ goes through a peak value before reaching its steady value.

Fig. 16(a) and (b) are used to determine the development of the recirculation length L_R, given in Fig. 17. This length is defined by the location in the wake relative to the sphere, where the fluid velocity in the wake equals the value of the sphere velocity. On Fig. 17 the recirculation length steadily converges for both simulation methods but a discrepancy of 13% is noticed on the steady state value.

As the Stokes number is considered to be high ($St = 240$), the contribution to the velocity field due to spanwise displacements of the particle is presumably weak. Indeed, it is found that the lateral particle displacements are not distinguishable from numerical noise, so the comparison with a fixed sphere in a stream can be made. According to the numerical results of Kim et al. [21], the dimensionless recirculation length behind a fixed sphere is $L_R/d_p \simeq 1.4$ in the Reynolds number range $250 < Re_p < 300$. Both simulation methods show convergence to higher values than the one of Kim et al. With similar fixed sphere configurations, Johnson and Patel [19] provide details on averaged velocities in the near wake, and the maximum velocity in fluid is found to be $|u|_m/u_\infty = 1.22$. This fixed-sphere value is found to be closely framed by the LB and the 1F values on steady state (see Fig. 16(a) (1F Method) and (b) (LB Method)).

Figs. 15–17 show remarkable differences in the details of the flow field of the two types of simulations. Fig. 15 shows that the near-particle flow field of the LB simulation exhibits more detailed structure than that of the 1F simulation. Figs. 16 and 17 show that although the upstream field is practically identical between the two approaches, slight discrepancies appear in the wake development following the type of simulation.

The detailed structure of the flow field is highly sensitive to the implementation of the boundary conditions and these are completely different for the two simulations. For the 1F method the boundary condition is directly linked to the numerical scheme. For the LB method, besides the adaptive force-field method, a range of boundary condition approaches is available (e.g. see [28]), each with its own advantages and disadvantages. The current test reveals that a detailed examination of the impact of the boundary condition on the structure of the flow field at high Re_p is justified. This, however, exceeds the purpose
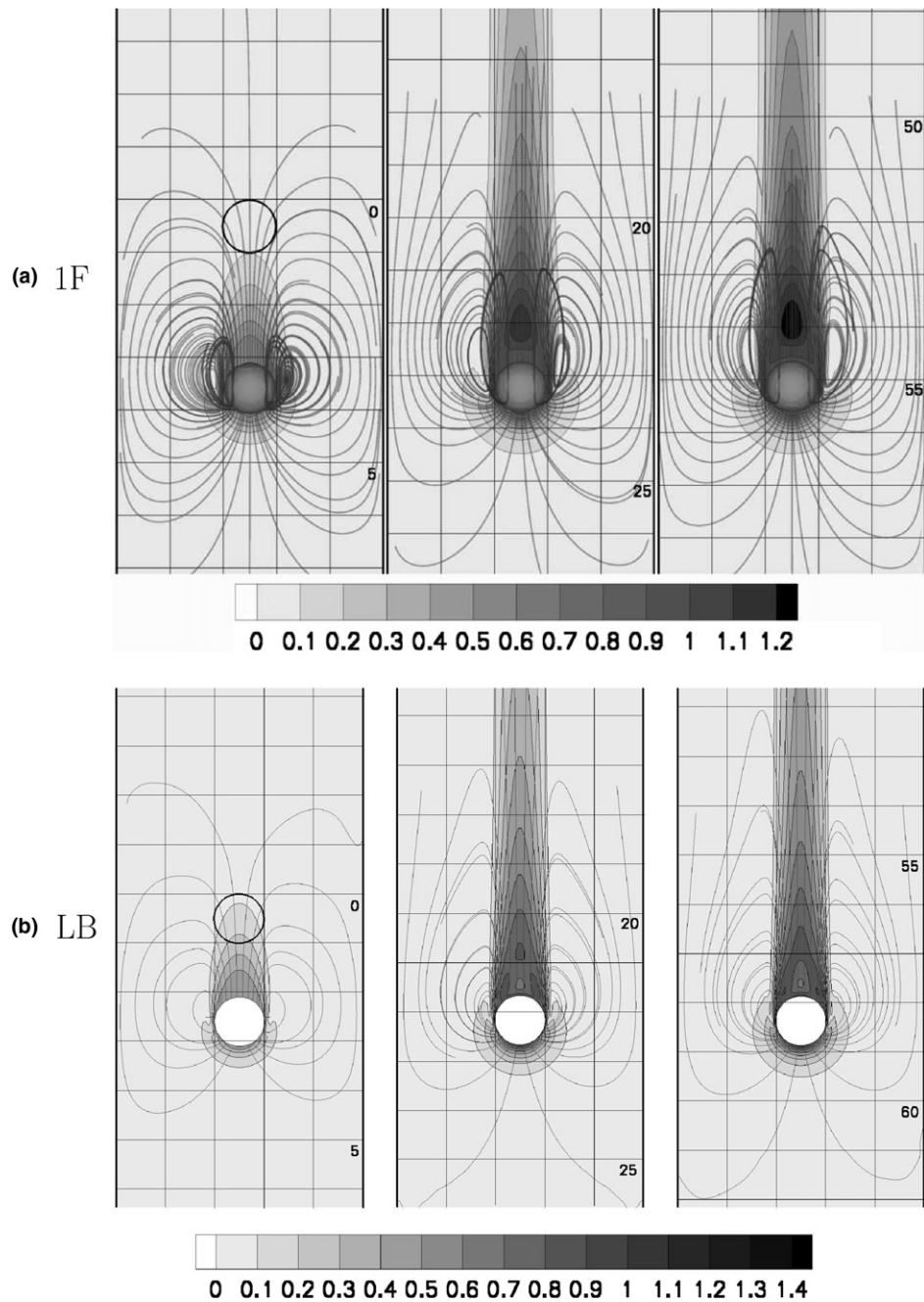
Fig. 15. Flow field slices, $Re_p = 280$, 1F (top) and LB (bottom) simulation methods.

of the current paper. Furthermore, the comparison to the external data shows that the global performance of both methods can be regarded satisfactory, certainly in light of the high Reynolds number considered.

4.3.3. Onset of wake instability

An important issue is that the predicted axisymmetric topology is not broken along the particle trajectory, irrespective of the method used. Furthermore the non-averaged experimental data showed that the particle sedimented without diverging from a straight trajectory. These facts are necessary to argue the lack of instabilities in the wake, but at this time, experiments do not provide much more clues about the fluid topology. Otherwise, a reason why the wake remains stable is that with both of the methods, the small spanwise dimensions of the domain and the symmetric initial conditions may suppress the development of wake oscillations. Generally speaking, it is shown that in the range $250 < Re_p < 300$, the flow past a fixed sphere experiences a transition from steady planar-symmetric to unsteady planar-symmetric topologies [19]. The global topology of the simulated flow fields does not show such transitions, but we try here to detect instabilities at a lower level.
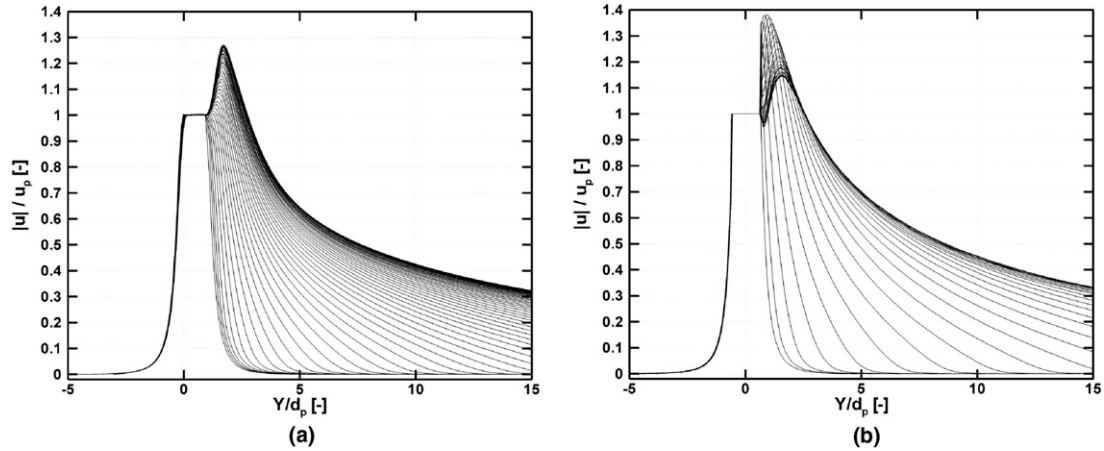
Fig. 16. Axial distribution of velocity magnitude $|\mathbf{u}(x_a, z_a, y, t)|/u_p(t)$, plotted versus the axial position Y/d_p expressed in the frame of reference attached to the sphere, with time t ranging from 0.0375 to 0.125 (s) by steps of 0.0375 (s). 1F method (a), LB method (b).
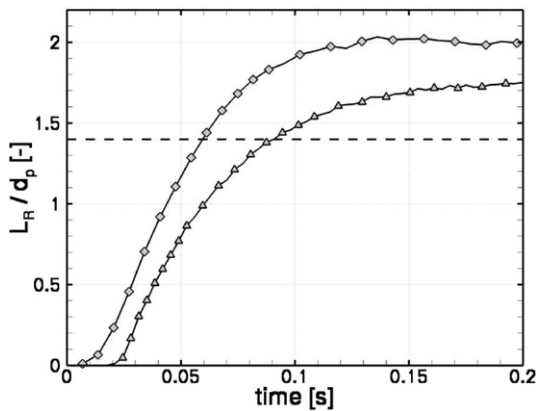

Fig. 17. Dimensionless recirculation length L_R/d_p versus time, 1F method (△), LB method (◇), fixed sphere value (dashed line).

Table 5
Characteristic scales: 1F, LB, references

	1F method	LB method	Reference
Settling velocity u_∞ (m/s)	0.310	0.337	0.316 [25]
Maximum velocity $|u|_m/u_\infty$ (–)	1.27	1.15	1.22 [19]
Backflow length L_R/d_p (–)	1.74	2.00	1.4 [21]
Strouhal number St (–)	0.104	0.169	0.137 [21]

tures in the wake is clearly periodic. This makes possible to evaluate the Strouhal number $St = fd_p/u_\infty$ of the flow where f is the frequency associated to the structures development.

In Table 5 where the comparisons between fixed-sphere data and the two simulation methods are summarized, it is made clear that the predicted Strouhal numbers are of the same order of magnitude as in literature.

5. Conclusions

We have described the 1-fluid method as a way to perform direct numerical simulation of particulate flow. The associated techniques have been designed to make the 1F method fully implicit. This results in excellent numerical stability properties. Several benchmark simulations were done to demonstrate good numerical consistency with the literature. The sensitivity of the method to a number of numerical parameters was studied. Criteria are provided
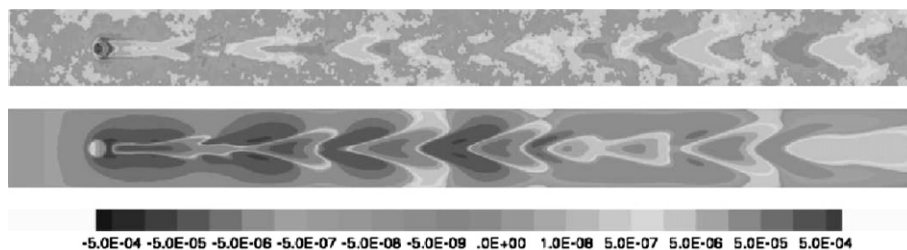
The first clue for oscillations must appear with out-of-plane motions, i.e. that for an axisymmetric wake, the velocity field $V_z(x, y, 0)$ is theoretically zero. Consequently our investigation is focused on the two-dimensional velocity field $V_z(x, y, 0)/u_\infty$ which is depicted in Fig. 18 for the two simulation methods. A zero-centered logarithmic scale is set so as to make contrast between the zone where $V_z(x, y, 0)/u_\infty$ could be alternatively negative or positive. Fig. 18 shows an interesting coincidence between 1F and LB simulations methods, since analogous 'V-shape' structures are predicted. The spatial distribution of these struc-

-5.0E-04 -5.0E-05 -5.0E-06 -5.0E-07 -5.0E-08 -5.0E-09 .0E+00 1.0E-08 5.0E-07 5.0E-06 5.0E-05 5.0E-04

Fig. 18. $V_z(x, y, 0)/u_\infty$, LB method (top), 1F method (bottom).

for the choice of these parameters that make the method operational in a wide range of flow configurations.

Validation of the 1F method has been done by comparing simulation data of the motion of a single sedimenting sphere with the experimental data of Ten Cate et al. [4]. The experimental dataset consists of the particle trajectory, flow fields and velocity time series at $1 < Re_p < 32$. The good reproduction of the experimental data showed that the 1F method is an accurate method for simulations of transient particle motion.

To extend the range of particle Reynolds and Stokes numbers, simulations of the sedimentation of a metal bead at $Re_p = 280$ have been performed with both the 1F and the LB method. The experimental data of Mordant et al. [25], consisting of the transient sphere velocity, was used as an external reference. For this case, both methods gave globally good results. At a converged resolution, the 1F method gave a slight underprediction of the steady state velocity of 2%, while the LB simulations gave an overprediction of 6%.

The wake structure obtained with both simulation methods has been discussed in detail. The growth of the recirculation length during sedimentation was shown to be comparable for both methods. The steady state recirculation length showed to be somewhat larger than values reported in literature for a fixed sphere in the range $250 < Re_p < 300$. In both simulation methods, periodic structures were observed in the out-of-plane fluid velocity in the midplane of the simulation domain. These structures reveal the onset of wake instability. Literature values suggest that the transition from steady to unsteady flow occurs at $Re_p \simeq 250$ and the corresponding Strouhal number of the wake structure was of the same order as has been reported for fixed spheres. Nevertheless, the magnitude of the unsteady wake flow was too small to have an impact on the transient sphere motion, which remained fully rectilinear over the entire sedimentation trajectory, in agreement with the experimental observations of Mordant et al. [25]. Also, between the 1F and LB method local differences in details of the wake structure near the sphere were observed. At this moment no further investigations were done to examine these differences.

A comparison of the computational performance of the two methods has showed large discrepancies. The 1F method has showed very good numerical accuracy at low spatial resolution, but also showed to be computationally very intensive. The LB method has shown to be more than an order of magnitude faster in numerically efficiency at the cost of numerical accuracy, thus requiring high spatial resolution to achieve comparable accuracy as the 1F method.

Currently, we are working on two points to improve and extend the 1F method for multi-particle simulations: (i) efficient parallelization of the method is implemented to reduce the limitations of the large computational cost of the 1F method; (ii) for particle–particle or particle–wall interactions near contact, we are investigating methods to implement sub-grid lubrication forces.

References

[1] Brenner H. The slow motion of a sphere through a viscous fluid towards a plane surface. Chem Eng Sci 1961;16:242–51.

[2] Caltagirone JP, Breil J. Sur une méthode de projection vectorielle pour la résolution des équations de Navier–Stokes. C R Acad Sci Paris 1999;327(2b):1179–84.

[3] Caltagirone JP, Vincent S. Sur une méthode de pénalisation tensorielle pour la résolution des équations de Navier–Stokes. C R Acad Sci Paris 2001;329(2b):607–13.

[4] Ten Cate A, Nieuwstad CH, Derksen JJ, Van den Akker HEA. Particle imaging velocimetry experiments and lattice-Boltzmann simulations on a single sphere settling under gravity. Phys Fluids 2002;14(11):4012–25.

[5] Ten Cate A, Derksen JJ, Portela LM, Van den Akker HEA. Fully resolved simulations of colliding monodisperse spheres in forced isotropic turbulence. J Fluid Mech 2004;519:233–71.

[6] Chen S, Doolen GD. Lattice Boltzmann method for fluid flows. Ann Rev Fluid Mech 1998;30:329–64.

[7] Chopard B, Droz M. Cellular automata modeling of physical systems. 1st ed. Cambridge: Cambridge University Press; 1998.

[8] Derksen JJ, Van den Akker HEA. Large eddy simulations on the flow driven by a Rushton turbine. AIChE J 1999;45(2):209–21.

[9] Eggels JGM, Somers JA. Numerical simulation of free convective flow using the lattice-Boltzmann scheme. Int J Heat Fluid Flow 1995;16:357–64.

[10] Elasmi L, Berzig M, Feuillebois F. Stokes flow for the axisymmetric motion of several spherical particles perpendicular to a plane wall. Z Angew Math Phys 2003;54:304–27.

[11] Fortin M, Glowinski R. Méthode de lagrangien augmenté. Application à la résolution numérique des problèmes aux limites. Paris: Collection méthodes mathématiques de l'informatique, Dunod; 1982.

[12] Glowinski R, Pan TW, Hesla TI, Joseph DD, Periaux J. A fictitious domain approach to the direct numerical simulation of incompressible viscous flow past moving rigid bodies: application to particulate flow. J Comput Phys 2001;169(1):363–427.

[13] Pan TW, Glowinski R. Direct simulation of the motion of neutrally buoyant circular cylinders in plane Poiseuille flow. J Comput Phys 2002;181:260–79.

[14] Harlow FH, Welch JE. Numerical calculations of time dependent viscous incompressible flow of fluid with a free surface. Phys Fluids 1965;8(12):2182–9.

[15] Hill RJ, Koch DL, Ladd AJC. The first effects of fluid inertia on flows in ordered and random arrays of spheres. J Fluid Mech 2001;448:213–41.

[16] Hill RJ, Koch DL, Ladd AJC. Moderate-Reynolds-number flows in ordered and random arrays of spheres. J Fluid Mech 2001;448:243–78.

[17] Hirsh C. Numerical computation of internal and external flows. Computational methods for inviscid and viscous flows, vol. 2. Wiley-Interscience Publishers; 1990.

[18] Hu HH, Patankar NA, Zhu MY. Direct numerical simulations of fluid/solid systems using the arbitrary Lagrangian/Eulerian technique. J Comput Phys 2001;169(2):427–62.

[19] Johnson TA, Patel VC. Flow past a sphere up to a Reynolds number of 300. J Fluid Mech 1999;378(1):19–70.

[20] Khadra K, Angot P, Parneix S, Caltagirone JP. Fictitious domain approach for numerical modelling of Navier–Stokes equations. Int J Numer Meth Fluids 2000;34(1):651–84.

[21] Kim D, Choi H. Laminar flow past a sphere rotating in the streamwise direction. J Fluid Mech 2002;461(1):365–86.

[22] Ladd AJC. Numerical simulations of particulate suspensions via a discretized Boltzmann equation. Part 1. Theoretical foundation. J Fluid Mech 1994;271:285–309.

[23] Ladd AJC. Numerical simulations of particulate suspensions via a discretized Boltzmann equation. Part 2. Numerical results. J Fluid Mech 1994;271:311–39.

[24] Legendre D, Magnaudet J, Mougin G. Hydrodynamic interactions between two spherical bubbles rising side by side in a viscous liquid. J Fluid Mech 2003;497:133–66.

[25] Mordant N, Pinton JF. Velocity measurement of a settling sphere. Eur Phys J B 2000;18:343–52.

[26] Randrianarivelo N, Pianet G, Vincent S, Caltagirone JP. Numerical modelling of the solid particles motion using a new penalty method. Int J Numer Meth Fluids 2005;47:1245–51.

[27] Ritz JB, Caltagirone JP. A numerical continuous model for the hydrodynamics of fluid particle systems. Int J Numer Meth Fluids 1999;30:1067–90.

[28] Rohde M, Derksen JJ, Van den Akker HEA. Volumetric method for calculating the flow around moving objects in lattice-Boltzmann schemes. Phys Rev E 2002;65:056701.

[29] Shin S, Juric D. Modeling three-dimensional multiphase flow using a level contour reconstruction method for front tracking without connectivity. J Comput Phys 2002;180:427–70.

[30] Scardovelli R, Zaleski S. Direct numerical simulation of free-surface and interfacial flow. Ann Rev Fluid Mech 1999;31(1):567–603.

[31] Somers JA. Direct simulation of fluid flow with cellular automata and the lattice-Boltzmann equation. Appl Sci Res 1993;51:127–33.

[32] Soo SL. Fluid dynamics of multiphase systems. Waltham: Blaisdell Publishing Company; 1967.

[33] Succi S. The lattice Boltzmann equation for fluid dynamics and beyond. 1st ed. Oxford: Oxford University Press; 2001.

[34] Vincent S, Caltagirone JP, Lubin P, Randrianarivelo TN. An adaptative augmented Lagrangian method for three-dimensional multi-material flows. Comput Fluids 2004;33:1273–89.

[35] van der Vorst HA. BI-CGSTAB: a fast and smoothly converging variant of BI-CG for the solution of nonsymmetric linear systems. SIAM J Sci Stat Comput 1992;13(2):631–44.

[36] Youngs DL, Morton KW, Baines MJ. Time-dependent multimaterial flow with large fluid distortion. Numerical methods for fluid dynamics. New York: Academic Press; 1982.